

# Spin Evolution of Millisecond Magnetars with Hyperaccreting Fallback Disks: Implications for Early Afterglows of Gamma-Ray Bursts

Z. G. Dai<sup>1,2,\*</sup> and Ruo-Yu Liu<sup>1,2,\*</sup>

<sup>1</sup>*School of Astronomy and Space Science, Nanjing University, Nanjing 210093, China*

<sup>2</sup>*Key Laboratory of Modern Astronomy and Astrophysics (Nanjing University), Ministry of Education, China*

\*dzg@nju.edu.cn, ryliu@nju.edu.cn

## ABSTRACT

The shallow decay phase or plateau phase of early afterglows of gamma-ray bursts (GRBs), discovered by Swift, is currently understood as being due to energy injection to a relativistic blast wave. One natural scenario for energy injection invokes a millisecond magnetar as the central engine of GRBs, because the conventional model of a pulsar predicts a nearly constant magnetic-dipole-radiation luminosity within the spin-down timescale. However, we note that significant brightening occurs in some early afterglows, which apparently conflicts with the above scenario. Here we propose a new model to explain this significant brightening phenomena by considering a hyperaccreting fallback disk around a newborn millisecond magnetar. We show that for typical values of the model parameters, sufficient angular momentum of the accreted matter is transferred to the magnetar and spins it up. It is this spin-up that leads to a dramatic increase of the magnetic dipole radiation luminosity with time and thus significant brightening of an early afterglow. Based on this model, we carry out numerical calculations and fit well early afterglows of 12 GRBs assuming sufficiently strong fallback accretion. If the accretion is very weak, our model turns out to be the conventional energy-injection scenario of a pulsar. Therefore, our model can provide a unified explanation for the shallow decay phase, plateaus, and significant brightening of early afterglows.

*Subject headings:* accretion disks — gamma-rays: bursts — magnetic fields — stars: neutron

## 1. Introduction

The successful launch of the Swift satellite (Gehrels et al. 2004) has opened a new era of the study of cosmological gamma-ray bursts (GRBs). In this era, there have been many important discoveries led by Swift (Zhang 2007 and Gehrels et al. 2009 for recent reviews), one of which is the identification of a canonical X-ray afterglow light curve, described by broken power laws  $F_\nu(t) \propto t^{-\alpha}$  (Nousek et al. 2006; Zhang et al. 2006): an initial steep decay phase with  $\alpha \sim 3$  (or a steeper slope) extending to  $\sim 10^2 - 10^3$  s is followed by a shallow decay phase with  $\alpha \sim 0.5$  or a flatter slope. This shallow decay phase usually lasts  $\sim 10^3 - 10^4$  s. A subsequent normal decay phase has  $\alpha \sim 1.2$ , being in agreement with the standard afterglow model. No spectral evolution across the shallow-to-normal decay break is observed. A post-jet-break decay phase with  $\alpha \sim 2$ , predicted by the jet model, is sporadically observed following the normal decay phase. Besides these four phases, one or multiple X-ray flares also appear in nearly one half of GRB early afterglows. The observed X-ray flares typically have very steep rising and decaying slopes (Burrows et al. 2005; Falcone et al. 2007).

These observations suggest that the GRB central engine may be in a long-lasting activity for two reasons. On one hand, the rapid rising and decaying timescales and their distributions of X-ray flares require that the central engine restarts at a later time (Lazzati & Perna 2007). This conclusion can also be drawn from the fact that the peak time of the X-ray flare observed by Swift is nearly equal to the ejection time of the outflow from the central engine, by assuming that the decaying phase of an X-ray flare is due to the high latitude emission from a relativistic outflow (Liang et al. 2006).

On the other hand, the shallow decay phase of early afterglows is currently understood as being due to energy injection into a relativistic blast wave, assuming an injection luminosity  $L(t) \propto t^{-q}$  (Zhang et al. 2006; Nousek et al. 2006). One natural scenario invokes a strongly magnetic millisecond pulsar, which spins down through magnetic dipole radiation (Dai & Lu 1998a, 1998b; Zhang & Mészáros 2001). An early version of this scenario is that a newborn pulsar loses its rotational energy in the form of Poynting flux. Numerical calculations based on this version by Fan & Xu (2006), Yu & Huang (2009), and Dall’Osso et al. (2011) show that it provides a satisfactory fitting to the observed shallow decay phase. Furthermore, the observed lightcurve plateaus of the early X-ray afterglows from GRBs 050319 (Huang et al. 2007), 050801 (De Pasquale et al. 2007), 060729 (Grupe et al. 2007), 070110 (Troja et al. 2007), 080913 (Greiner et al. 2009), and 090515 (Rowlinson et al. 2010) indicate that  $q \simeq 0$ , a pulsar-type energy injection. A recent, more physical version of the energy injection scenario of a pulsar assumes that the pulsar may continuously eject an ultrarelativistic electron-positron-pair wind, interaction of which with a circum-burst medium leads to a

relativistic wind bubble (Dai 2004). The relativistic reverse shock emission from this bubble can fit observed shallow decays and even plateaus in some GRB afterglows (Yu & Dai 2007; Mao et al. 2010).

An alternative scenario for energy injection requires ejecta with a wide- $\Gamma$  (Lorentz factor) distribution from a newborn black hole (Rees & Mészáros 1998; Sari & Mészáros 2000), in which scenario the low- $\Gamma$  ejecta catch up with a blast wave when the high- $\Gamma$  ejecta are decelerated. Two features of this scenario are that all the materials with a wide- $\Gamma$  distribution are impulsively released from the central engine during the prompt emission phase and that the resulting reverse shock during the shallow decay phase is non-relativistic. On the contrary, the central engine activity is long-lasting in the energy injection scenario of a pulsar and the reverse shock is ultrarelativistic. This difference has some astrophysical implications for testing the two scenarios (Dai 2004; Yu et al. 2007; Corsi & Mészáros 2009).

The comparisons of the energy injection scenario of a pulsar with the observations (Lyons et al. 2010; Yu et al. 2010) show that the central engine of some GRBs may be a millisecond magnetar, a type of millisecond pulsar whose surface magnetic-field strength exceeds the critical one. The conventional magnetic-dipole-radiation model predicts  $q \simeq 0$  within the spin-down timescale. This naturally explains the shallow decay phase and plateaus ( $\alpha \sim 0$ ). As analyzed by Liang et al. (2007), however, we note that in some early afterglows  $\alpha$  is obviously smaller than zero. This requires that  $q < 0$ . In this paper we propose a new model to explain this significant brightening phenomena by considering a hyperaccreting fallback disk around a newborn millisecond magnetar. Zhang & Dai (2008, 2009) first investigated the properties of a hyperaccreting disk around a neutron star, and Zhang & Dai (2010) further studied the effects of a magnetar-strength magnetic field on the disk. The present paper focuses on the effects of a hyperaccreting fallback disk on spin evolution of a newborn millisecond magnetar.

This paper is organized as follows: section 2 describes both the generation of a GRB within the framework of a millisecond magnetar and the magnetar-disk interactions. Section 3 studies the magnetar’s spin evolution during fallback accretion analytically and numerically. We show that for typical values of the surface magnetic field strength, initial rotation period, and accretion rate, sufficient angular momentum of the accreted matter is transferred to the magnetar and spins it up. It is this spin-up that leads to a dramatic increase of the magnetic-dipole-radiation luminosity with time and thus significant brightening of an early afterglow. Section 4 fits the early afterglows of 12 GRBs in the relativistic pulsar wind bubble model proposed by Dai (2004) and reconsidered by Yu & Dai (2007). The final section presents a discussion and conclusions.

## 2. GRB Generation and Magnetar-Disk Interactions

### 2.1. Generation of a GRB

A millisecond magnetar has been one of the two leading models of central engines of long-duration GRBs (Usov 1992; Duncan & Thompson 1992; Thompson 1994; Wheeler et al. 2000; Thompson et al. 2004; Woosley 2011 for a recent review). This model assumes that the collapse and supernova explosion of a massive star at the end of its life leaves behind a rapidly-rotating neutron star with a period of  $\sim 1$  ms and an ultrastrong surface magnetic field of  $\sim 10^{15}$  G. An ultra-strong field may be produced by dynamo processes (Duncan & Thompson 1992; Akiyama et al. 2003; Thompson et al. 2005). Subsequent cooling of the magnetar leads to a wind, which has four phases (Thompson et al. 2004; Komissarov & Barkov 2008; Bucciantini et al. 2008, 2009; see Fig. 2 in Metzger et al. 2011 for recent results): (1) in  $\sim 1$  s after the explosion, the wind is driven by neutrino energy deposition, so it is matter-dominated. Its asymptotic velocity is only  $\sim 0.1c$ . (2) A few seconds later, the wind becomes magneto-centrifugally dominated. In this phase, it is still matter-dominated and non-relativistic. (3) A few seconds (perhaps  $\sim 2 - 5$  s) later after phase 2, the stellar mass-loss rate decreases sufficiently so that the wind is accelerated to a relativistic velocity possibly with Lorentz factor of  $\geq 100$  from the magnetar surface out to the light cylinder by magneto-centrifugal forces. It is the wind in phase 3 that may generate a GRB. This wind is initially highly magnetized. Its Lorentz factor evolves with radius as  $\propto r^{1/3}$  and eventually equals to the wind magnetization at the saturation radius (Drenkhahn 2002; Drenkhahn & Spruit 2002; also see Metzger et al. 2011). Beyond this radius, a series of internal collision-induced magnetic reconnection and turbulence events would occur (Zhang & Yan 2011). These events could have a highly radiative efficiency for producing a GRB. (4) At the end of the cooling epoch, both the neutrino luminosity and mass-loss rate decrease dramatically. The Lorentz factor of the wind increases to  $\gamma_w \sim 10^6$  and the millisecond magnetar enters its pulsar phase, in which its rotational energy is lost through the magnetic dipole radiation mechanism rather than the magneto-hydrodynamical mass-loss process.

A newborn millisecond magnetar cools on the Kelvin-Helmholtz timescale ( $t_{\text{KH}}$ ) by radiating its gravitational binding energy via neutrinos. Thus, the duration of a GRB powered by the magnetar is nearly equal to  $t_{\text{KH}}$ . For a non-rotating proto-neutron star,  $t_{\text{KH}}$  is about 30 s (Pons et al. 1999). For the millisecond magnetar, however, rapid rotation may decrease the overall neutrino luminosity and average energy by a factor of at most  $\sim 5 - 6$  (Thompson et al. 2005). If the same amount of gravitational binding energy is assumed to be liberated under the zeroth-order approximation, we expect that  $t_{\text{KH}}$  should increase by the same factor. In the millisecond magnetar model, therefore, the maximum duration of a GRB is unlikely to be longer than  $\sim 200$  s.

## 2.2. Magnetar-Disk Interactions

The materials ejected during the supernova explosion must have a velocity distribution, some of which fail to achieve escape velocity and eventually fall back onto the central millisecond magnetar. The minimum free-fall time of fallback matter is denoted by  $t_{\text{fb}}$ . This time might be extended because the falling matter needs to overcome the resistance of a low-density neutrino-heated bubble (MacFadyen et al. 2001). If this effect is neglected,  $t_{\text{fb}}$  corresponds to the minimum radius around which matter starts to fall back,  $r_{\text{fb}} = (2GMt_{\text{fb}}^2)^{1/3} \simeq 1.0 \times 10^{10} (M/1.4M_{\odot})^{1/3} (t_{\text{fb}}/50 \text{ s})^{2/3} \text{ cm}$ , where  $M$  is the magnetar mass. However, the matter staying around  $r_{\text{fb}}$  cannot be immediately accreted. This is because a relativistic wind (with luminosity of  $L_{\text{w}} \sim 10^{49} - 10^{51} \text{ erg s}^{-1}$ ) from the central magnetar may exert an outward ram pressure, which stops fallback accretion. Once  $L_{\text{w}}$  decreases dramatically just at  $t_{\text{KH}}$ , fallback accretion may be able to proceed. Therefore, we obtain the time when fallback accretion is expected to start,  $t_0 = \max(t_{\text{fb}}, t_{\text{KH}}) \sim 10^2 \text{ s}$ . This time is similar to the one from numerical simulations of MacFadyen et al. (2001). For simplicity, we set  $t_0 = 100 \text{ s}$  in the following calculations.

Following MacFadyen et al. (2001) and Zhang et al. (2008), we parameterize the fallback accretion rate

$$\dot{M} = (\dot{M}_{\text{early}}^{-1} + \dot{M}_{\text{late}}^{-1})^{-1}, \quad (1)$$

where

$$\dot{M}_{\text{early}} = 10^{-3} \eta t^{1/2} M_{\odot} \text{ s}^{-1}, \quad (2)$$

and

$$\dot{M}_{\text{late}} = 10^{-3} \eta t_1^{13/6} t^{-5/3} M_{\odot} \text{ s}^{-1}. \quad (3)$$

Here  $\eta \sim 0.01 - 10$  is a factor that accounts for different explosion energies (smaller  $\eta$  corresponds to a more energetic explosion), and  $t_1 \sim 200 - 10^3 \text{ s}$  is the time at which the mass accretion rate starts to drop (longer  $t_1$  for smaller  $\eta$ ). For  $t \gg t_1$ , equation (1) shows the late-time fallback accretion behavior follows  $\dot{M} \propto t^{-5/3}$ , as suggested by Chevalier (1989). Assuming that  $M_0$  is the initial baryonic mass of the magnetar, from equation (1), we obtain the stellar total baryonic mass at time  $t$ ,

$$M_b(t) = M_0 + \int_0^t \dot{M} dt. \quad (4)$$

Because a non-negligible fraction of this mass becomes binding energy and is radiated away in the form of neutrinos (as discussed by Lattimer & Prakash 2001), the time-dependent gravitational mass of the accreting magnetar with radius  $R_s$  is

$$M = M_b(t) \left[ 1 + \frac{3}{5} \frac{GM_b(t)}{R_s c^2} \right]^{-1}. \quad (5)$$

Since fallback matter has sufficient angular momentum, a geometrically-thin hyperaccreting disk forms around a magnetar, similar to the black hole disk of Chen & Beloborodov (2007). One main difference between these two types of disk is that the black hole disk extends to the innermost stable orbit but the magnetar disk is truncated at some radius by the magnetic field. This inner termination radius is one of the most pivotal physical quantities for the magnetar-disk interactions, as it affects the flow of energy and angular momentum in the accretion process. According to the popular viewpoint (Davidson & Ostriker 1973; Illarionov & Sunyaev 1975), since it is fixed around the magnetospheric radius, the inner termination radius increases smoothly across the corotation radius as the mass accretion rate decreases. Thus, once the inner termination radius is beyond the corotation radius, matter may be ejected from the system by the super-Keplerian magnetosphere, that is, the disk is in the propeller regime. This viewpoint was recently adopted to explore the spin evolution of a newborn millisecond magnetar and propose a propeller-powered supernova as a new mechanism for supernovae (Piro & Ott 2011).

We next define three useful radii within the accretion disk. The first radius is the corotation radius at which the Keplerian angular velocity ( $\Omega_K$ ) is equal to the rotation angular velocity of the central magnetar ( $\Omega_s$ ),

$$r_c = \left( \frac{GM}{\Omega_s^2} \right)^{1/3}. \quad (6)$$

The second radius is the magnetospheric radius defined by

$$r_m = \left( \frac{\mu^4}{GMM^2} \right)^{1/7}, \quad (7)$$

where  $\mu = B_0 R_s^3$  is the magnetic dipole moment of the magnetar and  $B_0$  is the surface magnetic field. The third radius is the distance from the stellar center to the light cylinder,

$$R_L = \frac{c}{\Omega_s}. \quad (8)$$

Within this radius, the vertical magnetic field component of the disk is assumed to have the dipolar form,  $B_z = \mu/r^3$ . In addition, the fastness parameter is defined as the ratio of the stellar rotation frequency to the Keplerian angular velocity at the magnetospheric radius,

$$\omega = \frac{\Omega_s}{\Omega_K(r_m)} = \left( \frac{r_m}{r_c} \right)^{3/2}. \quad (9)$$

The accretion disk is assumed to be truncated at  $r = r_m$ . If  $r_m < r_c$ , the matter at  $r_m$  is accreted onto the magnetar along some magnetic field lines and forced to corotate

with the magnetar, so that angular momentum of the accreted matter is always transferred to the magnetar. This provides a positive torque for the magnetar,  $\tau_0 = \dot{M}\sqrt{GMr_m}$ . If  $r_m \geq r_c$  (viz., in the propeller phase), however, the accreted matter at  $r_m$  initially rotates at the Keplerian angular frequency and immediately at the stellar angular velocity by the “magnetic slingshot” mechanism. This propeller effect thus leads to a negative torque exerted on the magnetar,  $\tau_0 = \dot{M}\sqrt{GMr_m}(1 - \omega)$ .

For  $r > r_m$ , the differential motion between the Keplerian disk and the magnetar generates an azimuthal field component,  $B_\phi$ . Wang (1995) derived some different expressions for  $B_\phi$  that are dependent on the field dissipation mechanisms. Here we adopt a simple but physically plausible expression for  $B_\phi$  as a function of radial distance (Livio & Pringle 1992; Wang 1995; Rappaport et al. 2004; Kluźniak & Rappaport 2007),

$$B_\phi = B_z \left(1 - \frac{\Omega_K}{\Omega_s}\right) = \left(\frac{\mu}{r^3}\right) \left[1 - \left(\frac{r_c}{r}\right)^{3/2}\right]. \quad (10)$$

The magnetic torque exerted on the magnetar by the disk is given by

$$\begin{aligned} \tau_M &= - \int_{r_m}^{R_L} r^2 B_\phi B_z dr \\ &= - \int_{r_m}^{R_L} \frac{\mu^2}{r^4} \left[1 - \left(\frac{r_c}{r}\right)^{3/2}\right] dr \\ &= -\frac{\mu^2}{9} \left(\frac{3}{r_m^3} - \frac{3}{R_L^3} - 2\sqrt{\frac{r_c^3}{r_m^9}} + 2\sqrt{\frac{r_c^3}{R_L^9}}\right) \\ &= -\frac{\mu^2}{9r_m^3} \left(3 - 3\epsilon^2 - \frac{2}{\omega} + \frac{2\epsilon}{\omega}\right), \end{aligned} \quad (11)$$

where  $\epsilon = (r_m/R_L)^{3/2}$ . Therefore, the net torque exerted on the magnetar by the accretion disk reads

$$\tau_{\text{acc}} = \tau_0 + \tau_M = n(\epsilon, \omega)(\dot{M}\sqrt{GMr_m}) = n(\epsilon, \omega)\frac{\mu^2}{r_m^3}, \quad (12)$$

where  $n(\epsilon, \omega)$  is the dimensionless torque parameter,

$$n(\epsilon, \omega) = \begin{cases} (2 - 2\epsilon + 6\omega + 3\epsilon^2\omega)/(9\omega), & \text{for } \omega < 1, \\ (2 - 2\epsilon + 6\omega + 3\epsilon^2\omega - 9\omega^2)/(9\omega), & \text{for } \omega \geq 1. \end{cases} \quad (13)$$

Please note that neither  $\tau_0$  nor  $n(\epsilon, \omega)$  connects smoothly from  $\omega < 1$  to  $\omega > 1$  in our model. This is because for  $\omega < 1$  and  $\omega > 1$ , the system is in two different phases, the accretion phase and the propeller phase. Recently a discontinuity of the dimensionless torque parameter across  $\omega = 1$  was also noted by Tauris (2012). When  $r_m > R_L$  (viz.,  $\epsilon > 1$ ), the magnetar-disk interactions are so weak that  $\tau_{\text{acc}} = 0$ . In this case, the magnetar behaves as a normal pulsar, which spins down through magnetic dipole radiation.

### 3. Spin Evolution of the Magnetar

Spin evolution of the magnetar is given by the following differential equation,

$$\frac{d(I\Omega_s)}{dt} = \tau_{\text{acc}} + \tau_{\text{dip}}, \quad (14)$$

where  $I = 0.35MR_s^2$  is the stellar moment of inertia and  $\tau_{\text{dip}}$  is the torque due to magnetic dipole radiation,

$$\tau_{\text{dip}} = -\frac{\mu^2\Omega_s^3 \sin^2 \chi}{6c^3} = -\frac{\mu^2 \sin^2 \chi}{6R_L^3}, \quad (15)$$

with  $\chi$  being the inclination angle of the magnetic axis to the rotation axis. For moderately stiff to stiff equations of state for nuclear matter, the radius of a massive neutron star is nearly independent on the mass (Lattimer & Prakash 2001), so  $R_s$  is taken to be a constant in this paper.

#### 3.1. Asymptotic Analytical Solutions

Before carrying out numerical calculations on equation (14), we derive analytical solutions in three limiting cases. Generally, we have  $r_m \ll R_L$  or  $\epsilon \ll 1$ , so  $n(\epsilon, \omega)$  is simplified as

$$n(\epsilon, \omega) \simeq \frac{2}{9\omega} + \frac{2}{3} > \frac{8}{9}, \quad \text{for } \omega < 1, \quad (16)$$

and

$$n(\epsilon, \omega) \simeq \frac{3 - (3\omega - 1)^2}{9\omega} \leq -\frac{1}{9}, \quad \text{for } \omega \geq 1. \quad (17)$$

Hence, we obtain

$$\left| \frac{\tau_{\text{dip}}}{\tau_{\text{acc}}} \right| = \frac{\epsilon^2 \sin^2 \chi}{|6n(\epsilon, \omega)|} \ll 1, \quad (18)$$

and  $\tau_{\text{dip}}$  can be neglected compared to  $\tau_{\text{acc}}$  in equation (14). Then first, for  $\omega \ll 1$  (viz., slow rotators), we find  $n(\epsilon, \omega) \simeq 2/(9\omega)$  from equation (13). After further assuming a constant moment of inertia and neglecting the  $\dot{I}\Omega_s$  term in equation (14), we have

$$I \frac{d\Omega_s}{dt} \simeq \tau_{\text{acc}} \propto \dot{M}^{9/7} \Omega_s^{-1}. \quad (19)$$

Since  $\dot{M} \propto t^{1/2}$  at early times ( $t_0 < t < t_1$ ), equation (19) becomes

$$\Omega_s \propto t^{23/28}, \quad (20)$$

showing that the magnetar spins up at early times.



Second, in the case of  $\omega \sim 1$ , we obtain  $\Omega_s \sim \Omega_K(r_m) \propto r_m^{-3/2} \propto \dot{M}^{3/7}$ . Since  $\dot{M} \propto t^{-5/3}$  at late times, we find

$$\Omega_s \propto t^{-5/7}, \quad (21)$$

which is roughly consistent with an approximative solution to equation (14),  $\Omega_s \propto t^{-3/7}$ , if we also assume a constant moment of inertia and neglect the  $\dot{I}\Omega_s$  and  $\tau_{\text{dip}}$  terms as in the first case. This shows that the magnetar spins down.

Third, if  $\omega \gg 1$  (viz., fast rotators), we find  $n(\epsilon, \omega) \simeq -\omega$ . From equation (14) together with  $\dot{M} \propto t^{-5/3}$ , we have

$$\frac{d\Omega_s}{dt} = -K\Omega_s t^{-5/7}, \quad (22)$$

assuming that  $K$  is the coefficient. An integration to equation (22) leads to

$$\Omega_s = \Omega_s(t_1) \exp[-(7K/2)(t^{2/7} - t_1^{2/7})]. \quad (23)$$

This also implies that the magnetar spins down.

### 3.2. Numerical Results

Numerical integrations to equation (14) lead to spin evolution of the magnetar for different values of the model parameters (viz., surface magnetic field strength  $B_0$ , initial rotation period  $P_0$ ,  $\eta$ , and  $t_1$ ). This further provides the magnetic-dipole-radiation luminosity as a function of time<sup>1</sup>,

$$L_{\text{dip}} = \frac{\mu^2 \Omega_s^4 \sin^2 \chi}{6c^3} = 9.6 \times 10^{48} \text{ erg s}^{-1} \sin^2 \chi \left( \frac{\mu}{10^{33} \text{ G cm}^3} \right)^2 \left( \frac{P}{1 \text{ ms}} \right)^{-4}. \quad (24)$$

In our calculations, we take  $\sin^2 \chi = 0.5$ . For this value and smaller values of  $\sin^2 \chi$  (viz., weakly oblique rotators), the magnetar-disk interaction and dimensionless torque parameter are nearly identical to those for an aligned rotator (Wang 1997). The initial baryonic mass of a magnetar is assumed to be  $1.4M_\odot$  and the maximum gravitational mass is  $2.5M_\odot$ , beyond which the magnetar may become a black hole. We consider this value of the maximum mass of a neutron star for two reasons: (1) very stiff nuclear equations of state lead to the maximum mass of  $\sim 2.5M_\odot$  (Lattimer & Prakash 2001), and more importantly, (2) detections of the mass of the black widow pulsar, PSR B1957+20, give  $M_{\text{PSR}} = (2.40 \pm 0.12)M_\odot$  (van

---

<sup>1</sup>The coefficient in this equation (Shapiro & Teukolsky 1983) is by a factor of 4 smaller than that adopted in Dai & Lu (1998a).

Kerkwijk et al. 2011). In addition, a postmerger millisecond pulsar with mass  $\geq 2.5M_{\odot}$  has been suggested by Dai et al. (2006) to explain X-ray flares from a short-duration GRB. Figure 1 shows evolution of the stellar mass with time. We see that for typical values of  $\eta$  and  $t_1$  the stellar mass does not exceed the maximum mass during the fallback accretion.

We take the benchmark model parameters:  $P_0 = 3 \text{ ms}$ ,  $B_0 = 10^{15} \text{ G}$ ,  $\eta = 0.5$ , and  $t_1 = 400 \text{ s}$ . Figure 2 plots the stellar rotation period as a function of time for these benchmark values. We can see (from the red line in this figure) that the magnetar first spins up and then spins down. The evolutionary behaviors of the magnetar’s spin at early and late times are consistent with the asymptotic analytical solutions given by equations (20) and (21) respectively. The results for some other values of the model parameters are also shown in Figure 2. We also see that at late times the magnetar always spins down, being independent of what values the model parameters are taken to be. This is due to the fact that the fastness parameter  $\omega$  is close to (and somewhat larger than) unity at late times. At early times, however, the longer initial rotation period (or weaker surface magnetic field strength or larger  $\eta$  or longer  $t_1$ ), the more significant initial spin-up. Figure 3 shows the magnetic-dipole-radiation luminosity ( $L_{\text{dip}}$ ) as a function of time. We find a dramatic increase of  $L_{\text{dip}}$  for typical values of the model parameters.

We also calculate the magnetar’s rotation parameter  $\beta = T/|W|$ , where  $T = I\Omega_s^2/2$  and  $|W|$  is given by (Lattimer & Prakash 2001)

$$|W| \simeq 0.6Mc^2 \frac{GM/R_sc^2}{1 - 0.5(GM/R_sc^2)}, \quad (25)$$

which is shown in Figure 4. We see  $\beta < 0.14$  for typical values of the model parameters (except for the blue line in the right-upper panel), implying that some instabilities such as dynamical bar-mode instabilities and secular instabilities can be neglected. This is because the occurrence of these instabilities requires  $\beta > 0.27$  (Chandrasekhar 1969) and  $\beta > 0.14$  (Lai & Shapiro 1995) respectively.

#### 4. Fitting to Early Afterglows

The interaction of an ultrarelativistic wind from the millisecond magnetar with its ambient medium is in physics similar to the well-observed Crab Nebula. In order to explain the Crab Nebula, it was proposed (Rees & Gunn 1974; Kennel & Coroniti 1984; Begelman & Li 1992; Chevalier 2000) that a realistic, continuous wind from the Crab pulsar is ultrarelativistic and dominated by the kinetic energy flux of electron-positron pairs. From the viewpoint of evolution, even if this wind is initially Poynting flux-dominated, the fluctuating

component of the magnetic field in the wind can be dissipated by magnetic reconnection and used to accelerate the wind to an ultrarelativistic velocity (Coroniti 1990; Michel 1994; Kirk & Skæjaasen 2003). Recently, Aharonian et al. (2012) suggested that the acceleration should take place abruptly in the narrow cylindrical zone with radius between  $20R_L$  and  $50R_L$  and the wind’s Lorentz factor  $\gamma_w \sim 10^6$  to fit the spectral energy distribution of the pulsed high-energy  $\gamma$ -ray radiation from the Crab pulsar, even though this suggestion challenges current models on wind acceleration. In the case of a GRB afterglow, therefore, if the central engine is a millisecond magnetar, we assume that the magnetar’s wind with luminosity of  $L_w \simeq L_{\text{dip}}$  is accelerated to a Lorentz factor of  $\gamma_w \sim 10^6$  within a cylinder of radius much less than the typical deceleration radius ( $\sim 10^{16} - 10^{17}$  cm) of a relativistic GRB fireball in an interstellar medium. Please note that this assumption relaxes the requirement of abrupt acceleration of an ultrarelativistic wind suggested by Aharonian et al. (2012), but still keeps  $\gamma_w \sim 10^6$ . A similar value of  $\gamma_w$  has been adopted for some pulsar wind nebulae, e.g., G0.9+0.1 (Tanaka & Takahara 2011), and required by Suzaku observations of PSR B1259-63 (Uchiyama et al. 2009). As we find in our calculations, a large value of  $\gamma_w$  favors the occurrence of a lightcurve plateau or brightening of an early afterglow, although an accurate value of  $\gamma_w$  remains highly uncertain in the literature.

The interaction of an ultrarelativistic wind with its ambient medium leads to a relativistic wind bubble (Dai 2004; Yu & Dai 2007). This can be regarded as a relativistic version of the Crab Nebula. The relativistic wind bubble should include two shocks: a reverse shock that propagates into the cold wind and a forward shock that propagates into the ambient medium. Thus, there are four regions separated in the bubble by these shocks: (1) the unshocked medium, (2) the forward-shocked medium, (3) the reverse-shocked wind gas, and (4) the unshocked cold wind, where regions 2 and 3 are separated by a contact discontinuity. Dai (2004) analyzed the wind bubble’s dynamics and emission features, and found a plateau of the reverse shock emission light curve. Yu & Dai (2007) and Mao et al. (2010) carried out numerical calculations and confirmed such a plateau feature for typical values of the model parameters. This feature is due to the fact that for a magnetar without any accretion the wind luminosity  $L_w$  is nearly a constant at early times less than the typical spin-down timescale. As in sections 2 and 3, the fallback accretion spins up the magnetar, leading to an increase of the wind luminosity with time at early times, for typical values of the model parameters. It is thus expected that the reverse emission gives rise to significant brightening of an early afterglow.

Following Yu & Dai (2007), we calculate the dynamics of a relativistic wind bubble expanding in an interstellar medium (ISM) and the emission fluxes of forward and reverse shocks. As in Sari et al. (1998), we assume that  $p$  is the spectral index of the shock-accelerated electrons, and the electron and magnetic energy densities behind a shock are

fractions,  $\epsilon_e$  and  $\epsilon_B$ , of the total energy density of the shocked matter respectively. Of course, these parameters may be different for forward and reverse shocks, as the unshocked medium and the unshocked wind may have different magnetic fields and compositions. Figure 5 shows the light curves of forward and reverse shock emissions for the benchmark values of the model parameters (i.e.,  $P_0 = 3$  ms,  $B_0 = 10^{15}$  G,  $\eta = 0.5$ , and  $t_1 = 400$  s). From this figure, we can see significant brightening of an early afterglow, being due to a dramatic increase of the magnetar’s wind luminosity with time.

We search GRBs detected by Swift<sup>2</sup> and find the early-time significant brightening of 12 afterglows. Figure 6 provides fitting to these early afterglows for the assumed initial rotation period, surface magnetic field, and the parameters involved in the accretion rate. The required shock parameters are shown in Table 1. This table also presents the stellar gravitational mass at  $10^6$  s [i.e.,  $M(10^6 \text{ s})$ ], the maximum value of the rotation parameter ( $\beta_{\text{max}}$ ), and the minimum magnetospheric radius ( $r_{m,\text{min}}$ ) for each of 12 GRBs. We can see  $M(10^6 \text{ s}) < 2.5M_{\odot}$ ,  $\beta_{\text{max}} < 0.14$ , and  $r_{m,\text{min}} > R_s$ . In addition,  $R_L = c/\Omega_s = 47.7(P/1 \text{ ms}) \text{ km}$  is much greater than  $R_s$ . These ensure that our model is self-consistent. Figure 6 together with Table 1 shows that our model can well explain the significant brightening of 12 early afterglows. This explanation requires that the fallback accretion is sufficiently strong.

When the fallback accretion rate is so small that the magnetospheric radius  $r_m$  exceeds the light-cylinder radius  $R_L$  (viz.,  $\epsilon > 1$ ), both the fallback accretion and the propeller effect stop and the torque exerted on the magnetar by the accretion disk disappears. Meanwhile, the magnetar spins down only via the magnetic dipole radiation mechanism, which has been shown to be able to explain the shallow decay phase or the plateau phase of early afterglows (Dai & Lu 1998a, 1998b; Zhang & Mészáros 2001; Dai 2004; Yu & Dai 2007; Mao et al. 2010). In this case, therefore, our present model turns out to be the conventional energy injection scenario of a pulsar.

## 5. Discussion and Conclusions

Several physical explanations of the shallow decay phase or the plateau phase of early afterglows discovered by Swift include energy injection invoking a long-lasting central engine, energy injection from ejecta with a wide- $\Gamma$  distribution, two-component jets, dust scattering, varying microphysical parameters, and so on (see Zhang 2007). The two leading scenarios are based on energy injection to a relativistic blast wave. The first scenario invokes a millisecond

---

<sup>2</sup>[http://www.swift.ac.uk/xrt\\_curves/](http://www.swift.ac.uk/xrt_curves/)

magnetar, while the second scenario in fact requires a stellar-mass black hole. Thus, these two scenarios have different central engines. Three astrophysical implications are discussed to test them.

First, in the first scenario, the magnetic field in the reverse-shocked region of a relativistic wind bubble consists of two components: a large-scale toroidal field and a random field. If the toroidal field dominates over the random component, one would expect high polarization of an early afterglow during the shallow decay phase, as discussed by Dai (2004). This could be used to distinguish between the relativistic-wind-bubble model and the other explanations including the second scenario.

Second, the compositions of winds in the two scenarios are also different: the wind is lepton-dominated in the first scenario and baryon-dominated in the second scenario. Yu et al. (2007) studied the dynamics of winds and calculated the corresponding high-energy photon emission by considering synchrotron radiation and inverse Compton scattering of electrons. Even though in the two scenarios there is a plateau (or a bump) in high-energy light curves during the X-ray shallow decay phase, the first scenario predicts more significant high-energy gamma-ray afterglow emission than the second scenario does. This is because a considerable fraction of the injecting energy in the first scenario is shared by a relativistic long-lasting reverse shock and the reverse-shock energy is almost carried by leptons (electrons and positrons), while the energy of a nonrelativistic reverse shock is mainly carried by baryons in the second scenario.

Third, if the initial period of a newborn magnetar is as small as  $\sim 1$  ms and even smaller, then the stellar rotation parameter  $\beta$  may be larger than 0.14 (e.g., the blue line in the right-upper panel of Figure 4). In this case, some instabilities such as dynamical bar-mode instabilities and secular instabilities could not only be motivated so that they affect the stellar spin evolution, but also the resultant gravitational waves would be detectable with the future advanced-LIGO detector for a nearby GRB. Meanwhile, the magnetar’s rotational energy could be injected to a post-burst blast wave via magnetic dipole radiation, leading to the shallow decay phase of an early afterglow (Corsi & Mészáros 2009).

To summarize. It is well known that the conventional model of a pulsar predicts a nearly constant magnetic-dipole-radiation luminosity within the spin-down timescale. This provides an explanation for the shallow decay phase or the plateau phase of early afterglows. However, we note that significant brightening occurs in some early afterglows, which apparently conflicts with the conventional model. In order to explain this significant brightening phenomena, we here investigate the effect of a hyperaccreting fallback disk on the spin evolution of a newborn millisecond magnetar. We show that for typical values of the model parameters, sufficient angular momentum of the accreted matter is transferred to

the magnetar and spins it up. It is this spin-up that leads to a dramatic increase of the magnetic-dipole-radiation luminosity with time and thus significant brightening of an early afterglow. Furthermore, we carry out numerical calculations and fitted well early afterglows of 12 GRBs assuming sufficiently strong fallback accretion. Furthermore, It is worth noting that if the accretion is very weak, our present model turns out to be the previously-proposed energy injection scenario of a pulsar. Therefore, our model can provide a unified explanation for the shallow decay phase, plateaus, and significant brightening of early afterglows. In addition, possible detections of high polarization, gravitational waves, and/or high-energy gamma-rays during the shallow decay phase would be used to test this model in the future.

We thank the referee for useful comments and X.-D. Li and S. Rappaport for helpful discussions. This work was supported by the National Natural Science Foundation of China (grant no. 11033002).

## REFERENCES

- Aharonian, F. A., Bogovalov, S. V., & Khangulyan, D. 2012, *Nature*, 482, 507
- Akiyama, S., Wheeler, J. C., Meier, D. L., & Lichtenstadt, I. 2003, *ApJ*, 584, 954
- Begelman, M. C., & Li, Z. Y. 1992, *ApJ*, 397, 187
- Bloom, J. S., Perley, D. A., & Chen, H. W. 2006, *GRB Coordinates Network*, 5826
- Bucciantini, N., Quataert, E., Arons, J., Metzger, B. D., & Thompson, T. A. 2008, *MNRAS*, 383, L25
- Bucciantini, N., Quataert, E., Metzger, B. D., Thompson, T. A., Arons, J., & Del Zanna L. 2009, *MNRAS*, 396, 2038
- Burrows, D. N. et al. 2005, *Science*, 309, 1833
- Chandrasekhar, S. 1969, *The Silliman Foundation Lectures* (New Haven, CT: Yale Univ. Press)
- Chen, W. X., & Beloborodov, A. M. 2007, *ApJ*, 657, 383
- Chevalier, R. A. 1989, *ApJ*, 346, 847
- Chevalier, R. A. 2000, *ApJ*, 539, L45

- Chornock, R., Perley, D. A., & Cobb, B. E. 2009, GRB Coordinates Network, 10100
- Coroniti, F. V. 1990, ApJ, 349, 538
- Corsi, A., & Mészáros, P. 2009, ApJ, 702, 1171
- Cucchiara, A., & Tanvir, N. R. 2012, GRB Coordinates Network, 13217
- Dai, Z. G. 2004, ApJ, 606, 1000
- Dai, Z. G., & Lu, T. 1998a, A&A, 333, L87
- Dai, Z. G., & Lu, T. 1998b, Phys. Rev. Lett., 81, 4301
- Dai, Z. G., Wang, X. Y., Wu, X. F., & Zhang, B. 2006, Science, 311, 1127
- Dall’Osso, S. et al. 2011, A&A, 526, A121
- Davidson, K., & Ostriker, J. P. 1973, ApJ, 179, 585
- Drenkhahn, G. 2002, A&A, 387, 714
- Drenkhahn, G., & Spruit, H. C. 2002, A&A, 391, 1141
- Duncan, R. C., & Thompson, C. 1992, ApJ, 392, L9
- De Pasquale, M. et al. 2007, MNRAS, 377, 1638
- Falcone, A. D. et al. 2007, ApJ, 671, 1921
- Fan, Y. Z., & Xu, D. 2006, MNRAS, 372, 19
- Gehrels, N. et al. 2004, ApJ, 611, 1005
- Gehrels, N., Ramirez-Ruiz, E., & Fox, D. B. 2009, ARA&A, 47, 567
- Graham, J. F., Fruchter, A. S., Levan, A. J., et al. 2007, GRB Coordinates Network, 6836
- Greiner, J. et al. 2009, ApJ, 693, 1610
- Grupe, D. et al. 2007, ApJ, 662, 443
- Huang, K. Y. et al. 2007, ApJ, 654, L25
- Illarionov, A. F., & Sunyaev, R. A. 1975, A&A, 39, 185
- Kennel, C. F., & Coroniti, F. V. 1984, ApJ, 283, 694

- Kirk, J. G., & Skæjaasen, O. 2003, *ApJ*, 591, 366
- Kluźniak, W., & Rappaport, S. 2007, *ApJ*, 671, 1990
- Komissarov, S. S., & Barkov, M. V. 2008, *MNRAS*, 382, 1029
- Lai, D., & Shapiro, S. L. 1995, *ApJ*, 442, 259
- Lattimer, J. M., & Prakash, M. 2001, *ApJ*, 550, 426
- Lazzati, D., & Perna, R. 2007, *MNRAS*, 375, L46
- Liang, E. W. et al. 2006, *ApJ*, 646, 351
- Liang, E. W., Zhang, B. B., & Zhang, B. 2007, *ApJ*, 670, 565
- Livio, M., & Pringle, J. E. 1992, *MNRAS*, 259, 23P
- Lyons, N. et al. 2010, *MNRAS*, 402, 705
- MacFadyen, A. I., Woosley, S. E., & Heger, A. 2001, *ApJ*, 550, 410
- Mao, Z., Yu, Y. W., Dai, Z. G., Pi, C. M., & Zheng, X. P. 2010, *A&A*, 518, A27
- Metzger, B. D., Giannios, D., Thompson, T. A., Bucciantini, N., & Quataert, E. 2011, *MNRAS*, 413, 2031
- Milne, P. A., & Cenko, S. B. 2011, *GRB Coordinates Network*, 11708
- Michel, F. C. 1994, *ApJ*, 431, 397
- Nousek, J. A. et al. 2006, *ApJ*, 642, 389
- Piro, A. L., & Ott, C. D. 2011, *ApJ*, 736, 108
- Pons, J. A., Reddy, S., Prakash, M., Lattimer, J. M., & Miralles, J. A. 1999, *ApJ*, 513, 780
- Prochaska, J. X., Foley, R. J., Holden, B., et al. 2008, *GRB Coordinates Network*, 7397
- Rappaport, S., Fregeau, J., & Spruit, H. 2004, *ApJ*, 606, 436
- Rees, M. J., & Gunn, J. E. 1974, *MNRAS*, 167, 1
- Rees, M. J., & Mészáros, P. 1998, *ApJ*, 496, L1
- Rowlinson, A. et al. 2010, *MNRAS*, 409, 531



- Sari, R., Piran, T., & Narayan, R. 1998, *ApJ*, 497, L17
- Sari, R., & Mészáros, P. 2000, *ApJ*, 535, L33
- Shapiro, S. L., & Teuklosky, S. A. 1983, *Black Holes, White Dwarfs, and Neutron Stars* (New York: Wiley)
- Soderberg, A. M., Berger, E., & Ofek, E. 2005, *GRB Coordinates Network*, 4186
- Tanaka, S. J., & Takahara, F. 2011, *ApJ*, 741, 40
- Tauris, T. M. 2012, *Science*, 335, 561
- Thompson, C. 1994, *MNRAS*, 270, 480
- Thompson, T. A., Chang, P., & Quataert, E. 2004, *ApJ*, 611, 380
- Thompson, T. A., Quataert, E., & Burrows, A. 2005, *ApJ*, 620, 861
- Troja, E. et al. 2007, *ApJ*, 665, 599
- Uchiyama, Y. et al. 2009, *ApJ*, 698, 911
- Usov, V. V. 1992, *Nature*, 357, 472
- van Kerkwijk, M. H., Breton, R., & Kulkarni, S. R. 2011, *ApJ*, 728, 95
- Wang, Y.-M. 1995, *ApJ*, 449, L153
- Wang, Y.-M. 1997, *ApJ*, 475, L135
- Wheeler, J. C. et al. 2000, *ApJ*, 537, 810
- Woosley, S. E. 2011, arXiv:1105.4193
- Yu, Y., & Huang, Y. F. 2007, *Chin. J. Astron. Astrophys.*, 7, 669
- Yu, Y. W., Cheng, K. S., & Cao, X. F. 2010, *ApJ*, 715, 477
- Yu, Y. W., & Dai, Z. G. 2007, *A&A*, 470, 119
- Yu, Y. W., Liu, X. W., & Dai, Z. G. 2007, *ApJ*, 671, 637
- Zhang, B. 2007, *Chin. J. Astron. Astrophys.*, 7, 1
- Zhang, B. et al. 2006, *ApJ*, 642, 354

- Zhang, B., & Mészáros, P. 2001, ApJ, 552, L35
- Zhang, B., & Yan, H. R. 2011, ApJ, 726, 90
- Zhang, D., & Dai, Z. G. 2008, ApJ, 683, 329
- Zhang, D., & Dai, Z. G. 2009, ApJ, 703, 461
- Zhang, D., & Dai, Z. G. 2010, ApJ, 718, 841
- Zhang, W., Woosley, S. E., & Heger, A. 2008, ApJ, 679, 639

Table 1: Shock parameters and some other model parameters for fitting light curves of X-ray afterglows of some GRBs. The ISM number density, the magnetic field equipartition factor in the forward shock, the electron equipartition factor in the reverse shock, the spectral power-law index of forward-shocked electrons, the initial bulk Lorentz factor of the fireball and the bulk Lorentz factor of the relativistic wind are taken to be  $n = 1 \text{ cm}^{-3}$ ,  $\epsilon_{B,f} = 0.1$ ,  $\epsilon_{e,r} = 1 - \epsilon_{B,r}$ ,  $p_f = 2.2$ ,  $\gamma_0 = 300$ , and  $\gamma_w = 10^6$  for all GRBs (where the subscripts  $f$  and  $r$  denote forward and reverse shocks respectively). In this table,  $E_{\text{iso},51}$  is the postburst initial fireball energy in units of  $10^{51}$  ergs,  $M(10^6 \text{ s})$  is the mass of the accreting magnetar at  $10^6$  s,  $\beta_{\text{max}}$  is the maximum value of the magnetar’s rotation parameter, and  $r_{m,\text{min}}$  is the minimum value of the magnetospheric radius. The redshifts of GRBs are taken from GCN\*, while the redshifts of GRBs with no redshift measurement are artificially taken to be 1.0 (with superscript of  $a$ ).

GRB Name	$E_{\text{iso},51}$	$z$	$\epsilon_{e,f}$	$\epsilon_{B,r}$	$p_r$	$M(10^6 \text{ s})/M_{\odot}$	$\beta_{\text{max}}$	$r_{m,\text{min}}$ (km)
051016B	1	0.94	0.001	0.5	2.05	1.55	0.083	17.8
060109	1	1.0 <sup>a</sup>	0.01	0.001	2.5	1.80	0.049	23.5
060510A	1	1.0 <sup>a</sup>	0.01	0.5	2.1	2.43	0.084	17.7
061121	10	1.31	0.1	0.5	2.3	2.07	0.12	15.5
070103	0.1	1.0 <sup>a</sup>	0.01	0.5	2.05	1.42	0.097	16.7
070714B	1	0.92	0.01	0.0006	2.5	1.79	0.11	17.8
080229A	10	1.0 <sup>a</sup>	0.1	0.4	2.2	2.30	0.13	15.0
080310	1	2.43	0.1	0.002	2.2	1.92	0.11	17.5
091029	1	2.75	0.1	0.4	2.2	1.66	0.073	18.6
110213A	10	1.46	0.1	0.005	2.2	2.32	0.13	15.4
120118B	1	1.0 <sup>a</sup>	0.01	0.0001	2.5	2.29	0.053	20.7
120404A	10	2.87	0.1	0.002	2.2	2.07	0.083	17.8

[\*]: GRB 051016B (Soderberg et al. 2005), GRB 061121 (Bloom et al. 2006), GRB 070714B (Graham et al. 2007), GRB 080310 (Prochaska et al. 2008), GRB 091029 (Chornock et al. 2009), GRB 110213A (Milne et al. 2011), GRB 120404A (Cucchiara et al. 2012)

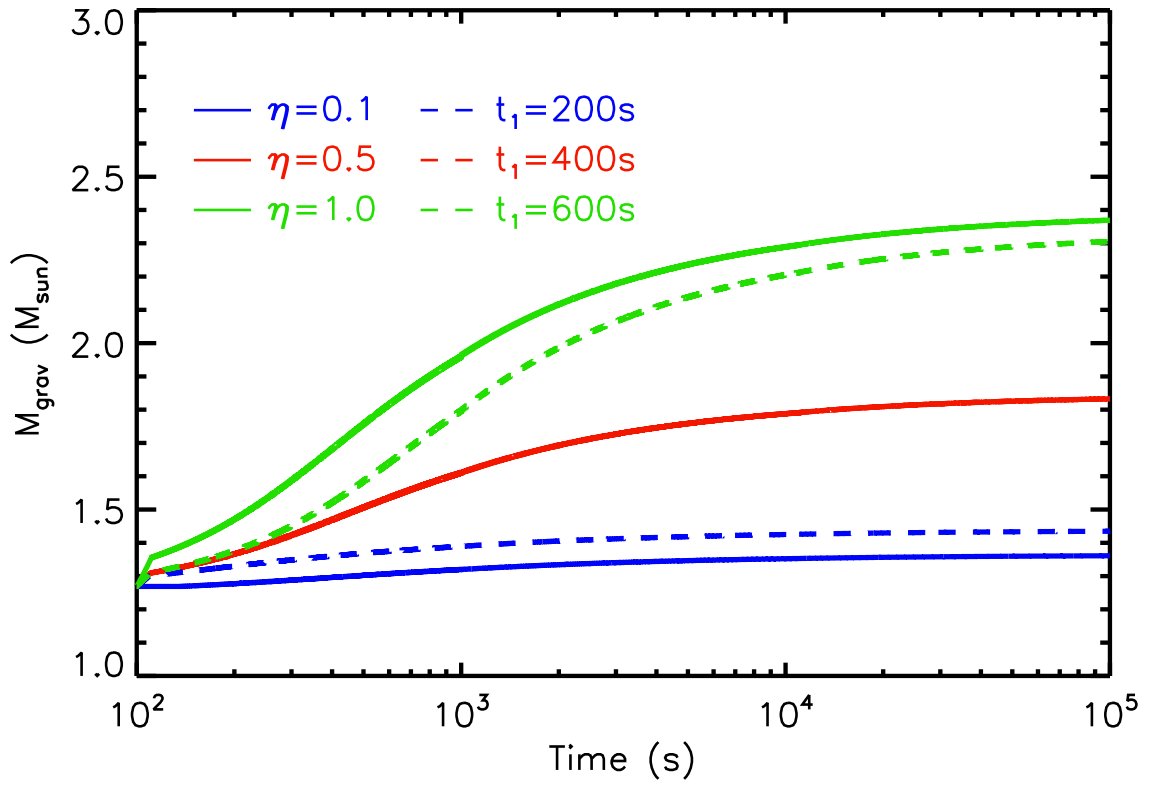


Fig. 1.— Gravitational mass evolution of a pulsar for different values of  $\eta$  (*solid lines*) and  $t_1$  (*dashed lines*). The initial baryonic mass of the pulsar is taken to be  $M_0 = 1.4M_\odot$ .

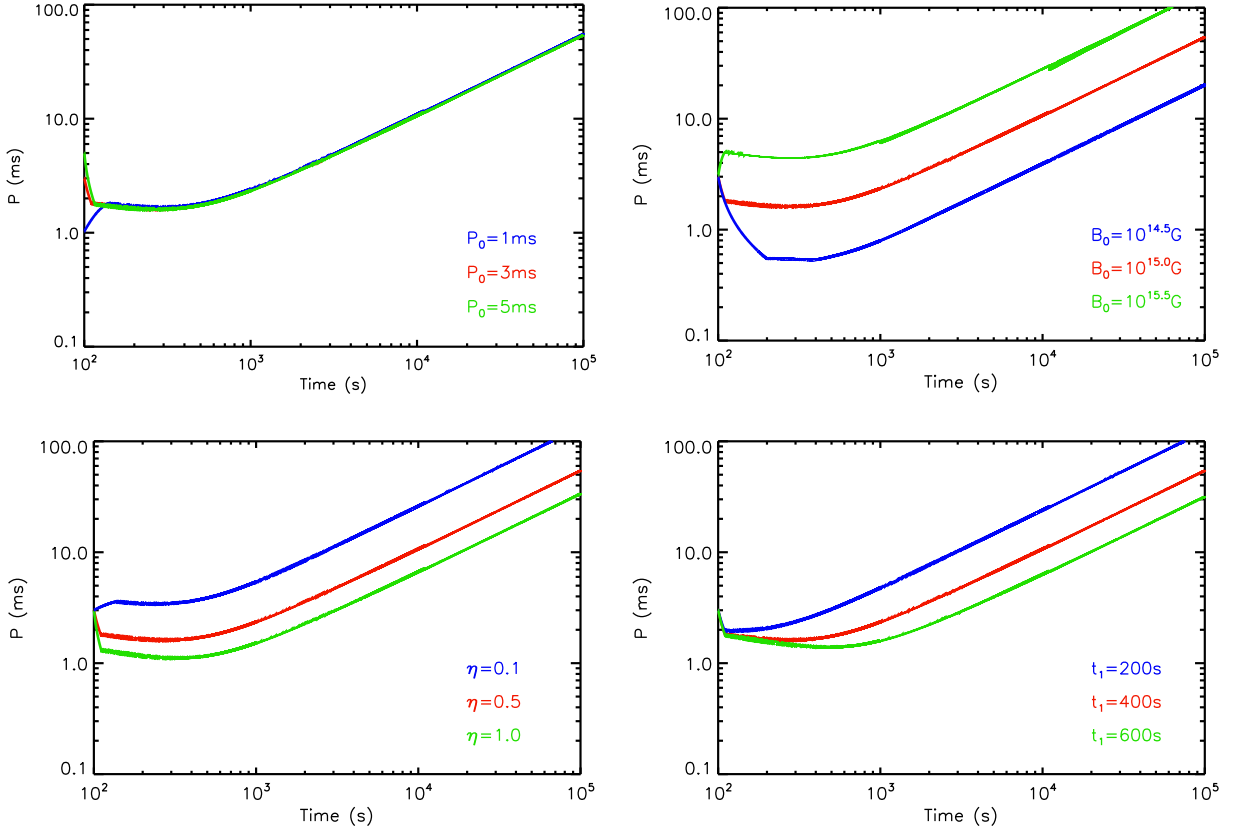


Fig. 2.— Spin evolution of a pulsar with time for different parameters. The initial baryonic mass and radius of the pulsar are taken to be  $M_0 = 1.4M_\odot$  and  $R_s = 12$  km respectively. The benchmark values of the other parameters such as the initial rotation period  $P_0$ , surface magnetic field strength  $B_0$ , dimensionless accretion rate  $\eta$  and transition time of accretion modes  $t_1$  are taken as follows:  $P_0 = 3$  ms,  $B_0 = 10^{15}$  G,  $\eta = 0.5$ , and  $t_1 = 400$  s. In each panel, we also plot spin evolution if one of the four parameters is changed while the other three parameters are fixed to be the benchmark values.

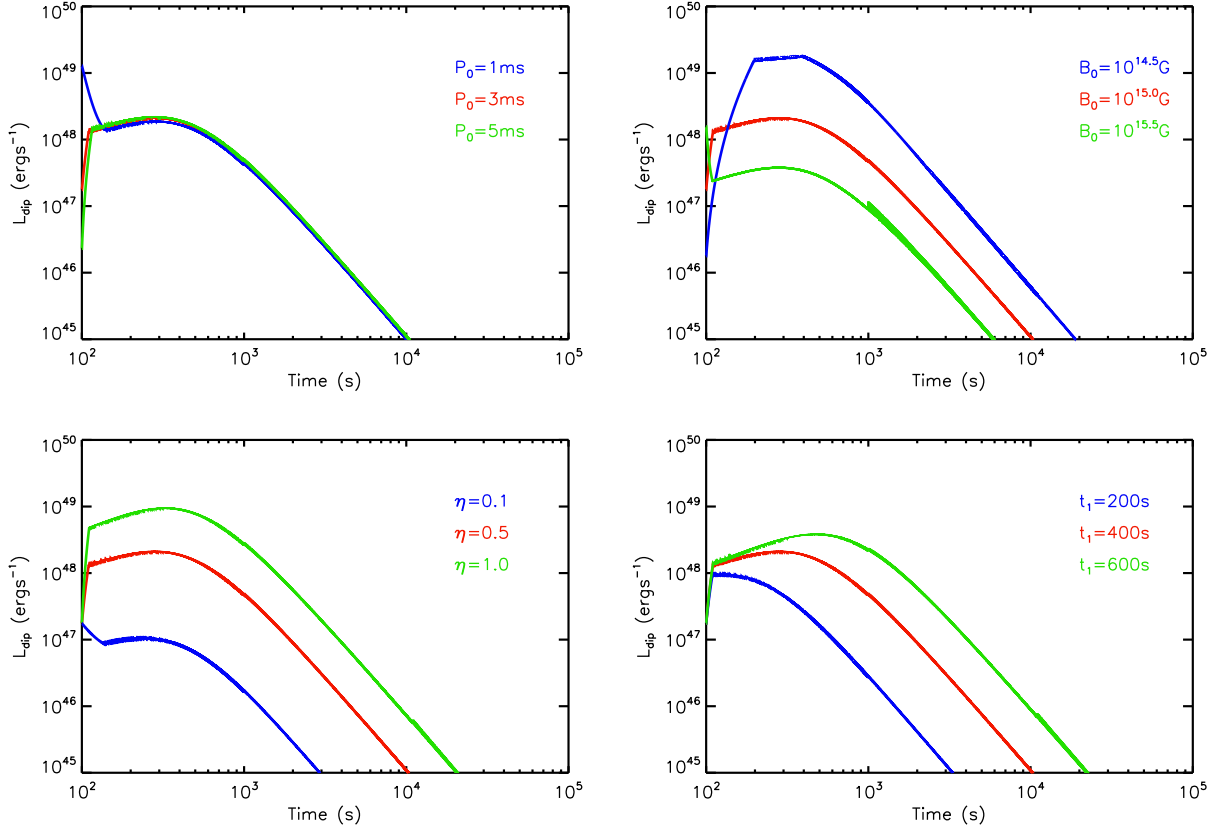


Fig. 3.— The same as Fig. 2 but for evolution of the magnetic-dipole-radiation luminosity  $L_{\text{dip}}$  with time.

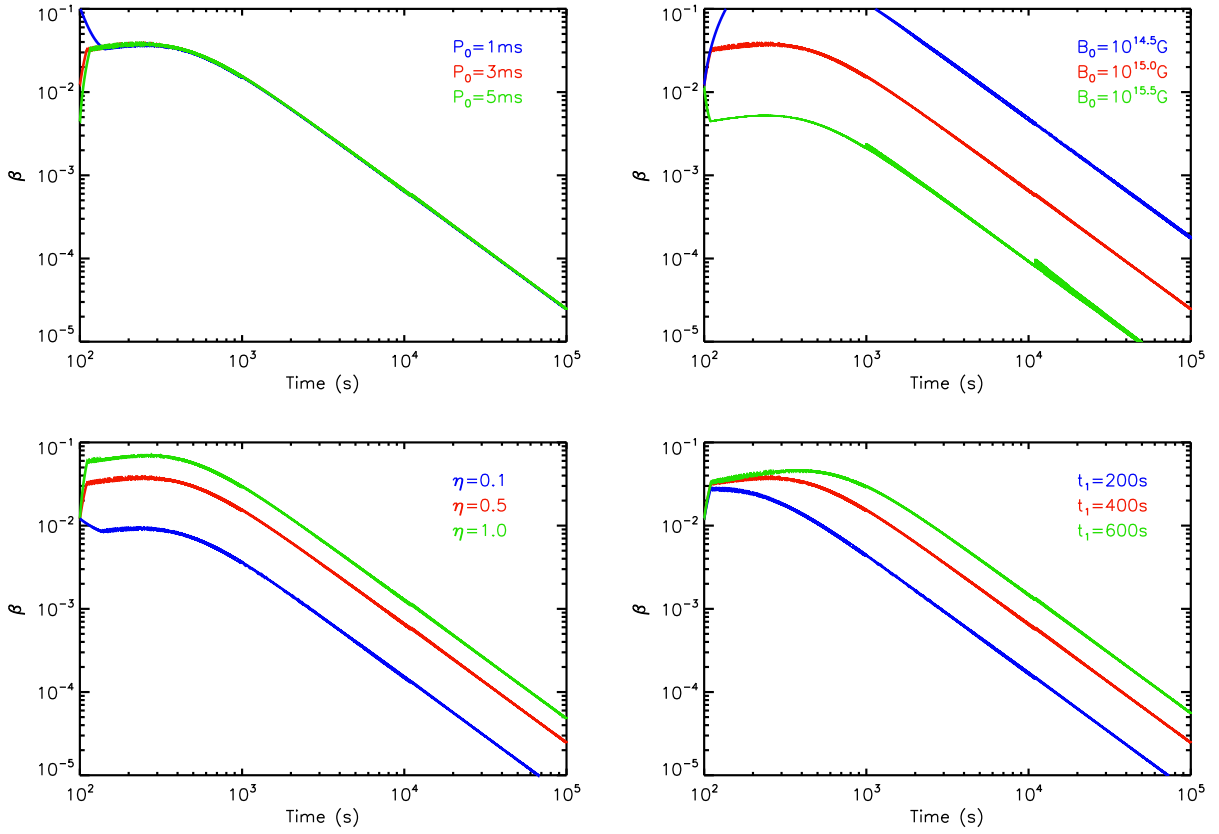


Fig. 4.— The same as Fig. 2 but for evolution of the pulsar’s rotation parameter  $\beta$  with time.

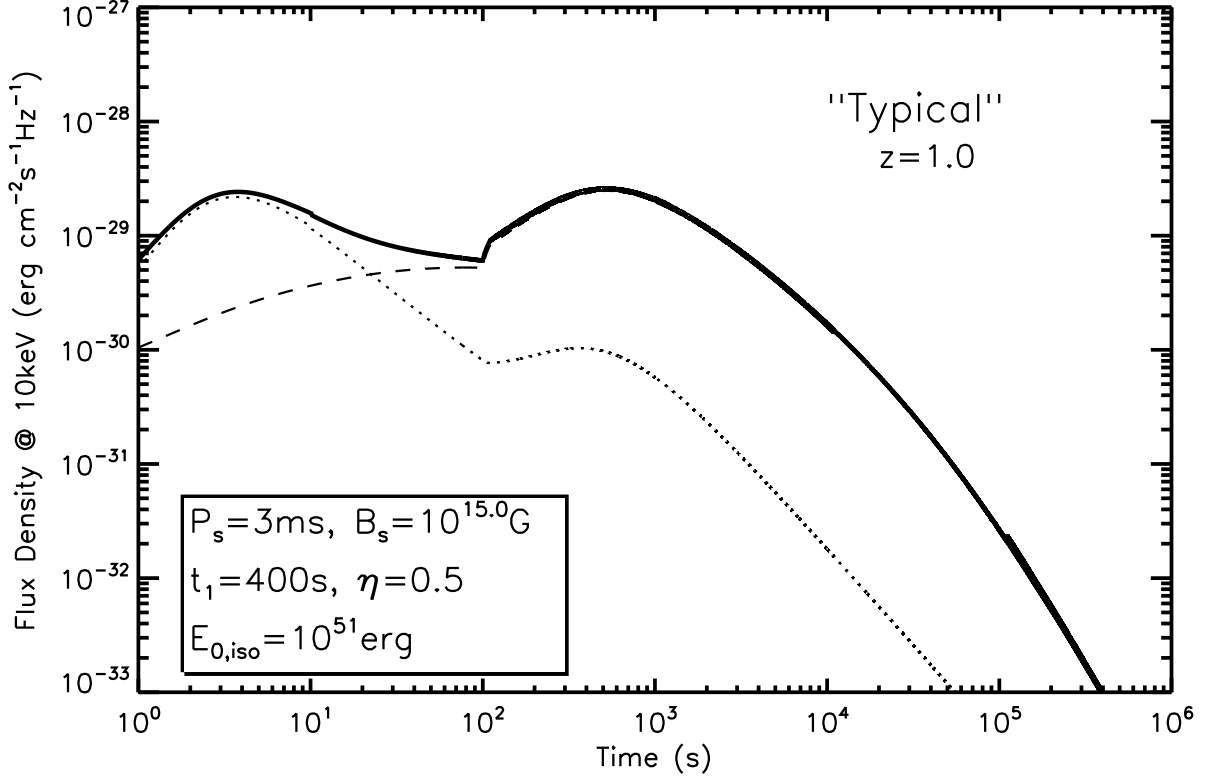


Fig. 5.— A typical light curve in our model. The dashed line is the contribution from the reverse shock emission in a relativistic wind bubble for the shock parameters  $\epsilon_{B,r} = 0.1$ ,  $\epsilon_{e,r} = 1 - \epsilon_{B,r} = 0.9$ , and  $p_r = 2.5$ , while the dotted line is the contribution from the forward shock emission in the ISM for the shock parameters  $\epsilon_{B,f} = \epsilon_{e,f} = 0.1$ , and  $p_f = 2.2$ . The initial bulk Lorentz factor of the GRB fireball is taken to be  $\gamma_0 = 300$  and that of the pulsar wind of  $e^\pm$  pairs is  $\gamma_w = 10^6$ . The thick solid line is the sum of the two components. The other parameters are labeled in the figure.



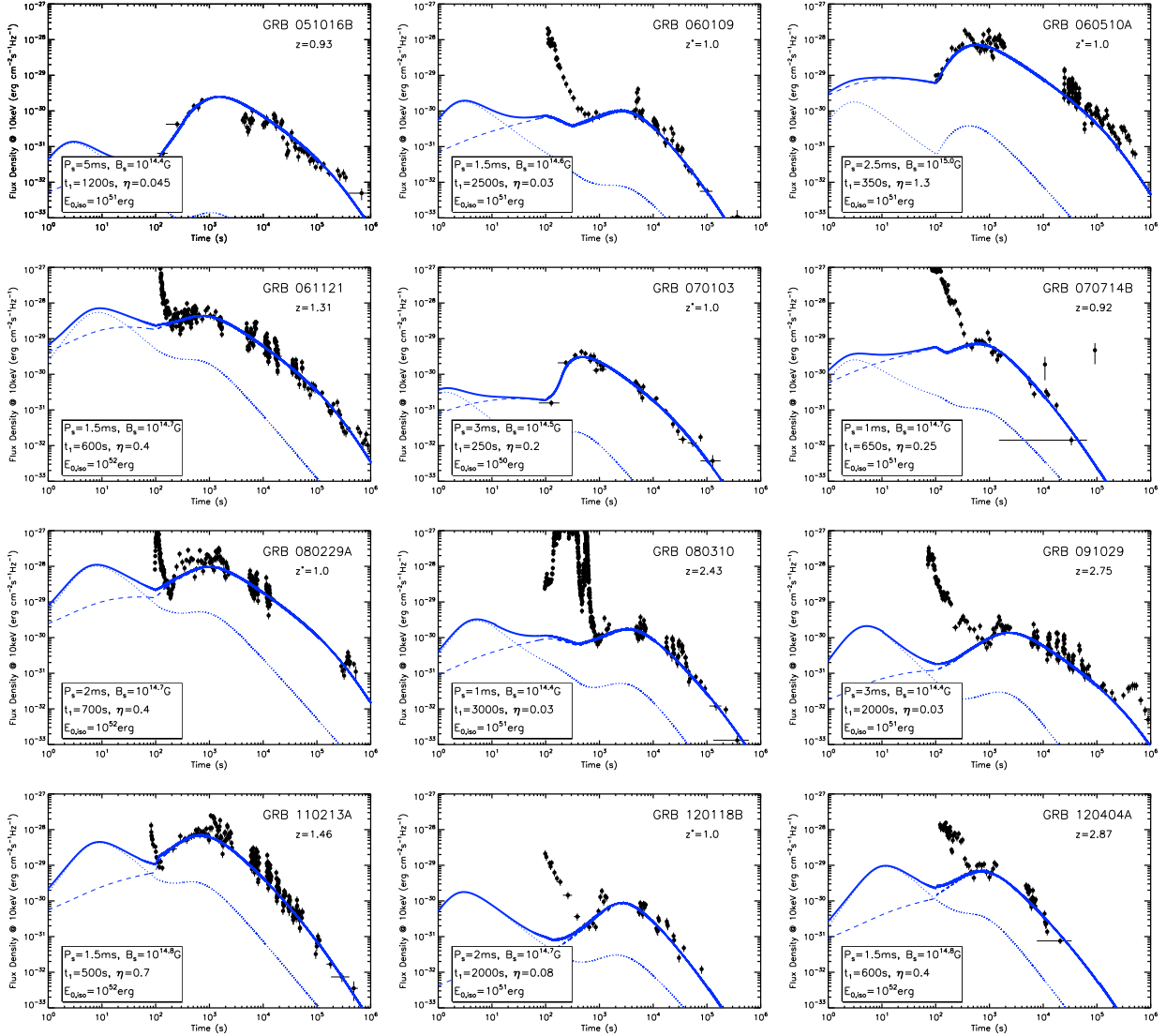


Fig. 6.— Fitting to the light curves of 12 X-ray afterglows with early-time significant brightening in our model. The black filled circles with error bars are Swift-XRT data. The blue dashed lines are contributions from reverse shocks, while the blue dotted lines represent contributions from forward shocks. The thick blue solid lines are the total fluxes of the two components. The shock parameters can be found in Table 1.